Biological and Medical Applications of Materials and Interfaces

Magnetic field-induced alignment of nanofibrous supramolecular membranes: a molecular design approach to create tissue-like biomaterials

Elham Radvar, Yejiao Shi, Salvatore Grasso, Charlotte J. C. Edwards-Gayle, Xitong Liu, Meagan S Mauter, Valeria Castelletto, Ian W. Hamley, Michael John Reece, and Helena S. Azevedo

Magnetic field-induced alignment of nanofibrous supramolecular membranes: a molecular design approach to create tissue-like biomaterials

Elham Radvar[†], Yejiao Shi,[†] Salvatore Grasso[‡], Charlotte J. C. Edwards-Gayle[§], Xitong Liu[#], Meagan S. Mauter[∂], Valeria Castelletto[§], Ian W. Hamley[§], Michael J. Reece[†] and Helena S. Azevedo[†]*

[†]School of Engineering and Materials Science & Institute of Bioengineering, Queen Mary University of London, Mile End Road, London E1 4NS, United Kingdom

[‡]School of Chemistry, Pharmacy and Food Sciences, University of Reading, Whiteknights, Reading, RG6 6AD, United Kingdom

[‡]Key Laboratory of Advanced technologies of Materials, Ministry of Education, School of Materials Science and Engineering, Southwest Jiaotong University, Chengdu, 61 0031, China

[#]Civil & Environmental Engineering, The George Washington University, 3520 Science and Engineering Hall, 800 22nd St NW, Washington, DC 20052, United States

[∂]Civil and Environmental Engineering, Stanford University, Y2E2, 473 Via Ortega, Room 311, Stanford, CA 94305, United States

ABSTRACT: A molecular design approach to fabricate nanofibrous membranes by self-assembly of aromatic cationic peptides with hyaluronic acid (HA) and nanofiber alignment under a magnetic field is reported. Peptides are designed to contain a block composed of four phenylalanine residues at the C-terminus, to drive their self-assembly by hydrophobic association and aromatic stacking, and a positively charged domain of lysine residues for electrostatic interaction with HA. These two blocks are connected by a linker with a variable number of amino acids and ability to adopt distinct conformations. Zeta potential measurements and circular dichroism confirm their positive charge and variable conformation (random coil, β-sheet or α-helix), which depend on the pH and sequence. Their self-assembly, examined by fluorescence spectroscopy, small-angle X-ray scattering and transmission electron microscopy, show the formation of fiber-like nanostructures in the micromolar range. When the peptides are combined with HA, hydrogels or flat membranes are formed. The molecular structure tunes the mechanical behavior of the membranes and the nanofibers align in the direction of magnetic field due to the high diamagnetic anisotropy of phenylalanine residues. Mesenchymal stem cells cultured on magnetically-aligned membranes elongate in direction of the nanofibers supporting their application for soft tissue engineering.

INTRODUCTION

Soft materials are pliable materials that easily deform as a result of the relatively weak non-covalent interactions that hold their individual building blocks together. Additional properties arising from these weak interactions are stimuli-responsive behavior and non-linear response to external mechanical forces (viscoelastic behavior).[1] Soft matter encompasses biological (living tissues) and a vast number of synthetic materials (gels, emulsions, foams, polymers, colloids). Biology uses multiscale self-assembly, the spontaneous formation of ordered mesoscopic structures from small building blocks, to create complex structural materials with hierarchical organization like collagen. Inspired by biology, supramolecular chemistry uses non-covalent forces to create molecular structures and materials mimicking biological counterparts. Mastering self-assembly and organization across the nano and microscales have been achieved in supramolecular peptide materials through molecular design and extrinsic forces,[2] but hierarchically oriented organization over large length scales (tissue size) is still challenging.

Manipulation of soft materials by external forces (heat, light, pressure, chemicals, electric, acoustic, gravitational and magnetic fields) is an attractive possibility to reshape their geometries/architectures and obtain new functions beyond their original properties.[3] The use of magnetic fields to actuate soft materials is promising to create orientational order in

biomaterials by controlling the magnitude and direction of the field.[4] Many molecular materials are endowed with diamagnetism,[5] a very weak form of magnetism that is induced by a change in the orbital motion of electrons due to an applied magnetic field. However, the force generated from the movement of the electrons is very small on the molecular level and its effects under normal magnetic fields is negligible due to the much stronger effect of Brownian motion. The magnetic response of soft materials can be enhanced by incorporating ferro- or para-magnetic materials into their structure. On the other hand, diamagnetism effect can exceed the effect of Brownian motion when large magnetic fields are applied (1-20 T). For example, aromatic rings have a high magnetic susceptibility due to the free movement of electrons around the ring. The magnetic susceptibility of a molecule is highly dependent on its volume and structure.[5] The stacking of aromatic rings (π-π interactions) in assembled molecules amplifies their magnetic susceptibility. Taking advantage of diamagnetic anisotropy of peptide bonds and aromatic rings, magnetic fields have been used to align peptide,[6-9] protein (collagen,[10] fibrin and outer membrane protein (Omp)[11]) fibers in the absence of ferro- or para-magnetic materials.

Our group has been developing soft membranes obtained by co-assembly of rationally designed peptides (peptide amphiphiles and multidomain peptides not containing aromatic residues) with hyaluronic acid (HA) without any external intervention.[12-14] Here we combine supramolecular and magnetic forces to fabricate self-assembling peptide/HA membranes and induce nanofiber alignment over the millimeter scale. We designed novel cationic aromatic peptides to self-assemble with HA and leverage the magnetic anisotropy of the peptides to control the nanofiber orientation by a magnetic field. These soft self-assembled membranes with aligned nanofibers can be used as scaffolds for engineering soft tissues and in mechanobiology studies.

EXPERIMENTAL SECTION

Peptide synthesis. All peptides were synthesized in an automated peptide synthesizer (Liberty Blue, CEM, UK) using standard 9-fluorenylmethoxycarbonyl (Fmoc) based solid phase chemistry. 4-methylbenzhydrylamine (MBHA) rink amide resin (100-200 mesh) was used as a solid support and Fmoc-protected amino acids were coupled using (4:4:4) equivalents of amino acids, 1-hydroxybenzotriazole hydrate (HOBt) and N,N′-diisopropylcarbodiimide (DIC). Fmoc groups were deprotected using 20% (v/v) piperidine in dimethylformamide (DMF). Before cleaving the peptide from the resin, the N-terminal of all peptides was capped with acetic anhydride (10% in DMF). The removal of the protecting groups of amino acid side-chains and peptide cleavage from the resin was achieved by incubating the peptide-bound resin with a mixture of trifluoroacetic acid (TFA)/ triisopropylsilane (TIS)/ water (95%/2.5%/2.5%). The cleaved peptide was collected and the resin washed with dichloromethane (DCM). The solutions were combined and reduced down in a rotary evaporator to a viscous solution. Cold diethyl ether was used to precipitate the peptide. After centrifuging, the supernatant was discarded and the solid allowed to dry overnight. The peptide mass was confirmed by electrospray ionization mass spectrometry (ESI-MS) using a single quadrupole mass detector (SQ Detector 2, Waters, UK). The crude peptide was purified using a

preparative reverse-phase C18 column (X-Bridge prep OBD, 5 μm, 30×150 mm column, Waters, UK) in a Waters 2545 Binary Gradient high-performance liquid chromatography (HPLC) system and using a gradient of ultrapure water/acetonitrile (0.1% TFA) as mobile phase. Fraction collection was carried out by mass detection and acetonitrile was removed from the collected fractions by rotary evaporator and then lyophilized. The purity of the peptides were confirmed by analytical HPLC (Alliance HPLC system coupled with 2489 UV/Vis detector, Waters, UK). Peptide samples (1 mg/ml) were injected into an analytical reverse-phase C18 column (XBridge analytic 3.5 μm, 4.6 x 150 mm, Waters, UK) and eluted through a gradient of water/acetonitrile (0.1% TFA) at 1 ml/min and detected at 220 nm.

Calculation of the diamagnetic susceptibility of the peptides. The diamagnetic anisotropy (DA) of the peptides was calculated based on the magnetic susceptibility of the amino acids and their spatial position with respect to one another using a recently developed computational method.[15] Briefly, the magnetic susceptibility tensor for amino acids was transformed to a single global coordinate followed by summing the tensors to build the net magnetic susceptibility tensor for the entire peptide structure, and the diamagnetic anisotropy was calculated for the peptides based on the eigenvectors and eigenvalues of the total magnetic susceptibility tensor for the peptide structure.[15] The molar and volumetric (dimensionless) diamagnetic anisotropy for the peptides are presented in **Table S1**.

Zeta-potential Measurements. Peptide solutions at different pHs (7, 10 and 11) were analyzed in a Nano-ZS Zetasizer (Malvern Instruments) for measuring their zeta potential. Solutions were prepared at 0.1 wt% in Milli-Q water and the pH adjusted with 0.1 M HCl and 0.1 M NH$_4$OH.

Circular Dichroism (CD) spectroscopy. Secondary structure of pure peptides was examined by CD spectroscopy using a PiStar-180 spectrometer from Applied Photophysics (Surrey, UK), under a constant flow of nitrogen (8 L min^{-1}) at a constant pressure value of 0.7 MPa. The measurements were recorded at 25 °C from 190 to 300 nm far-UV spectra. Peptide solutions were prepared in de-ionized water with a final concentration of 0.04 mM and the pH was adjusted to 3, 7, 10 and 11 with 0.1 M HCl and 0.1 M NH$_4$OH. Then, they were analyzed in a quartz cuvette with 1 mm path-length and all scans were performed in the steady state with a bandwidth of 1. The solvent spectrum was subtracted at each measurement and mean residue ellipticity obtained.

Fourier Transform Infrared (FTIR) Spectroscopy. To further investigate the secondary structure of the peptides, peptide solutions were prepared at concentration of 20 mg.ml^{-1} in D$_2$O (pH 7) and ND$_4$OD (pH 11). Then, the IR spectra of solutions were analyzed using Brukler Tensor 27 FTIR spectrometer using an attenuated total reflection (ATR) diamond crystal accessory (Bruker, Germany). The absorbance spectrum was measured in the range of 4000−400 cm^{-1} by averaging individual scans per sample at a resolution of 4 cm^{-1}.

Fluorescence Spectroscopy. The π-π interactions of the phenylalanine residues were analyzed on a LS55 fluorescence spectrometer (PerkinElmer, UK). Peptide solutions were prepared in the concentration range of 0.02 - 800 μM. The pH of peptide solutions was adjusted to 7 and 11 and then excited

at 210 nm and the fluorescence emission measured in the range of 280 - 400 nm[16].

Critical Aggregation Concentration (CAC). The CAC of the peptides was obtained by using the hydrophobic solvatochromic dye Nile Red[17]. Aqueous solutions of peptides with various concentrations, ranging from 0.02 to 82 µM, were prepared and added to the tubes containing dried Nile Red giving a final concentration of 1 µM of the dye. The mixture of peptides and Nile Red were left overnight to equilibrate. Fluorescence emission spectrum of each sample was recorded on a LS55 fluorescence spectrometer (PerkinElmer, UK) ranging from 580 to 720 nm with an excitation wavelength at 550 nm. The maximum intensity and the corresponding wavelength of each spectrum were plotted as a function of logarithm of peptide concentration.

Transmission Electron Microscopy (TEM). Peptide assemblies were imaged by TEM to analyze their morphology. Peptide aqueous solutions (0.05 wt%) were prepared and then 10 µL casted onto a carbon film-coated copper grid (400 mesh, Agar Scientific) followed by negative staining with 10 µL of uranyl acetate solution (2%, v/v) for 30 seconds. The excess staining solution was removed with a piece of filter paper and the grid allowed to dry at room temperature for at least 3 hours. Bright field TEM imaging was performed on a JEOL-1230 TEM operated at an acceleration voltage of 80 kV and the TEM images were recorded by a SIS Megaview III wide angle CCD camera.

Small Angle X-ray Scattering (SAXS). SAXS experiments were performed at the Diamond Synchrotron (Harwell, UK) on beamline B21. Solutions containing 0.5 wt% peptides in PCR tubes were loaded into the 96 well plate of an EMBL BioSAXS robot, and then injected via an automated sample exchanger into a quartz capillary (1.8 mm internal diameter) in the X-ray beam. The quartz capillary was enclosed in a vacuum chamber, in order to avoid air scattering. Data was collected using a Dectris EIGER 4M detector at a fixed camera length of 3.9 m with a wavelength $\lambda = 1$ Å. Data are presented as a function of $q = 4\pi \sin \theta / \lambda$, where 2θ is the scattering angle. Membranes were mounted in a custom-designed enclosed gel cell holder[18] for gels and pastes. All measurements were performed at 20 °C.

Membrane Assembly. The self-assembly of peptides with HA was tested by casting HA solutions on the bottom of a well-plate and peptide solutions were added on top at equal volume ratio. HA with different molecular weights (20, 60, 200 and 700 kDa) were tested and prepared at 2 wt% concentration except for 1.5 MDa HA where 1 wt% was used. The peptide solutions were prepared at 2 wt%. Peptides were left to incubate with HA at 37 °C overnight.

Scanning Electron Microscopy (SEM). The microstructure of the surface and cross-section of the obtained self-assembled materials (membrane or hydrogel) was examined by SEM. Samples were fixed with 2% glutaraldehyde in PBS. After cycles of washing with PBS, samples were progressively dehydrated using graded ethanol concentrations. Ethanol removal was performed using a critical point dryer (EMS 850, Electron Microscopy Sciences, USA). All samples were first coated with a gold layer (5-30 nm) using an Emitech SC7620 sputter coater (Quorum Technologies, UK) then imaged in a field emission gun scanning electron microscope (FEG SEM, Inspect F50, FEI, Netherlands). Analysis of aligned fibers in the membranes were performed by fast Fourier transform (FFT)

using ImageJ. Simply, the SEM images were used in ImageJ followed by processing the FFT function, giving the FFT image as output.

Mechanical Testing. Mechanical properties of all membranes were measured in a tensile testing machine. Membranes were formed in a mold with dimensions (5 mm × 15 mm) customized for this test allowing them to be clamped between tensile testing grips. The final dimensions of each sample were measured with a digital Calliper. To obtain the membrane thickness, each membrane was sandwiched between two coverslips and their thickness imaged using high resolution camera. The tensile test was performed in an Instron 3342 (UK) with a load cell of 10 N at the rate of 0.1 mm/s. Each test was repeated three times. After plotting the stress-strain curves, the elastic modulus was obtained by calculating the slope of the linear region of the curve. Statistical analysis was performed by one-way ANOVA using Bonferroni test for comparing membranes properties. (p-value: 0.1234 (ns), 0.0332 (*), 0.0021 (**), 0.0002 (***), <0.0001 (****)). The mechanical behavior of obtained hydrogels was analyzed by rheological measurements using a Discovery Hybrid Rheometer (DHR-3, TA Instruments, USA) fitted with a 8 mm diameter plate geometry (advanced Peltier plate, APP). Strain and frequency sweeps were examined at 1 Hz frequency and 0.1% strain, respectively. All experiments were carried out at 25 °C with a loading gap height set to 0.5 mm. Amplitude and frequency sweeps were performed on three repeats of samples.

Membrane Assembly under Magnetic Field. The effect of magnetic field on membrane fiber alignment was performed at 25 °C using a cryofree superconducting magnet (10 cm inner bore diameter, Cryogenic, UK) at fields of 12, 6 and 1 T. The alignment of fibers were confirmed using a graphite marker (lead pencil). Briefly, HA solutions were cast in the bottom of vials (or 96 well-plate for cell adhesion studies). Then, the peptide solution was added on top and the vial immediately inserted in the superconducting magnet at a set field. The membrane was allowed to form under the field for different periods of time. The formed membranes were removed after different time periods and inspected by SEM analysis as described above. Membranes were imaged with light microscopy (Olympus SC100 digital camera) with polarizing filters to assess their birefringence properties.

Cell Culture on the Membranes. Human-derived mesenchymal stem cells (hMSCs, passage number 6, PromoCell GmbH, Germany) were used for the cell adhesion studies. Cells were cultured in 75 cm² flask with cell density of 3×10^3 cells cm^{-2} and maintained in culture medium (DMEM, low glucose, GlutaMAX™) supplemented with 10% FBS, 1% Pen/Strep and 0.1% bFGF (FGF-Basic (AA 10-155) recombinant human protein, Thermo Fisher Scientific, UK). Flasks were incubated at 37 °C in an incubator supplied with 5% CO$_2$ flow. Medium of the cells was refreshed twice a week and cells were trypsinized when 80% confluency was reached.

All membranes were prepared using 1.5 MDa HA for the cell adhesion studies. RGDS-K$_2$A$_5$F$_4$/1.5 MDa HA membranes were also prepared with peptide solution containing 10% RGDS-K$_2$A$_5$F$_4$ and 90% of K$_2$A$_5$F$_4$ (**Figure S1**). All membranes were formed under sterile conditions except the ones prepared under magnetic field. Before MSC culture, the membranes were exposed to UV irradiation for 20 minutes. MSCs (30,000 cells per well (1.1 cm²)) were suspended in a culture medium (serum-

containing condition: DMEM supplemented with 10% FBS and 1% Pen/Strep; serum-free condition: DMEM supplemented with 1% Pen/Strep), seeded onto the membranes and incubated at 37 °C in an incubator supplied with 5% CO_2. They were left for attachment for 24 hours. The membranes were then washed with PBS and incubated in a permeabilization solution (5% v/v Triton X-100 (Sigma, USA), 0.14 wt% NaCl, 0.01 wt% $MgCl_2$ and 5 wt% sucrose) for 40 minutes at room temperature, washed twice with PBS and fixed using 4% paraformaldehyde (PFA, Sigma-Aldrich, Germany) for 15 minutes at room temperature. Cells cultured on the membranes were stained with 4,6-diamidino-2-phenylindole-dilactate (DAPI, nucleus staining, Invitrogen) and phalloidintetramethylrhodamine B isothiocyanate dyes (Phalloidin, cytoskeleton staining, Alexa Fluor™ 488 Phalloidin, Invitrogen). Briefly, for each staining, samples were incubated with 10 µl phalloidin in 1 ml PBS for 40 minutes following a three-cycle of PBS washing. Then DAPI staining was performed with 1 µl of dye in 1 ml of PBS with a 15 minutes incubation time. Cell monolayers cultured on the well-plate were used as a controls. Cell density and aspect ratio were both measured using the Fiji Image J software. The number of cells per mm^2 on the membranes was calculated by counting the nuclei (DAPI-stained) of the cells in a square of 0.5×0.5 mm dimensions and the aspect ratio was measured applying an ellipse fit to single cells and the ratio of the ellipse's dimensions acquired. Three replicates of membranes were imaged with epifluorescence microscopy (Leica DMi8 Epifluorescence). Statistical differences were obtained with GraphPad Prism 7 software (USA) using a two-way analysis of variance (ANOVA) with a Bonferroni's multiple comparison test (p-value: 0.1234 (ns), 0.0332 (*), 0.0021 (**), 0.0002 (***), <0.0001 (****)).

MSCs-cultured membranes were fixed and prepared for SEM as described above. Samples were coated with gold (Emitech SC7620 sputter coater, Quorum Technologies, UK) and imaged with a field emission gun scanning electron microscope (FEG SEM, Inspect F50, FEI, The Netherlands).

RESULTS AND DISCUSSION

Design and characterization of aromatic cationic peptides. The peptides designed in this work follow the $K_2X_nF_4$ template, with X serving as a linker segment between a positively charged lysine (K) domain and an aromatic block of four phenylalanine (F) residues. Phenylalanines were selected to establish π-π interactions between aromatic rings while the charged domain provides water solubility and imparts responsiveness to pH and (poly)electrolyte addition. The variable linker (X_n) is incorporated to control the degree of hydrogen bonding hence the secondary structure of the peptides. The number of alanine residues ($K_2A_3F_4$, $K_2A_5F_4$ and $K_2A_7F_4$) was investigated as well as different amino acids (serine and glycine: $K_2S_5F_4$ and $K_2G_7F_4$) (**Table 1**). Alanine residues were selected considering their α-helix propensity[19], while serine provides hydroxyl groups, through its side chain, for additional hydrogen bonding.[20] Glycine is achiral with a single hydrogen atom as its side chain.[21]

Peptides were successfully synthesized and purified (**Figure S1**) and their charge measured through zeta-potential (ζ-potential) analysis. All of the peptides showed positive zeta potential at pH 7, 10 and 11 (**Table 1**), as expected, but the zeta potential decreased with increasing pH as lysines become de-protonated (**Figure S2**). However, at pH 11 (over the pKa value of lysine side chains), the peptides showed a rather sharp drop in zeta potential compared to pH 10.
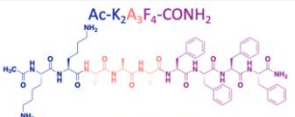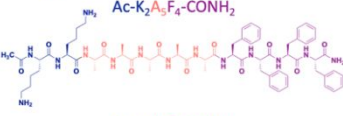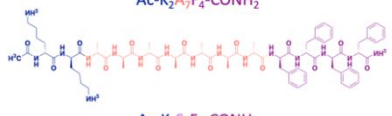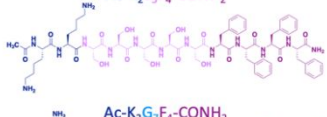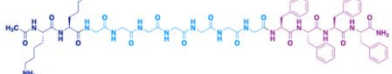
Aromatic dipeptides (e.g. diphenylalanine) or single aromatic amino acids (e.g. phenylalanine) are known to self-assemble into fibril nanostructures through well-ordered stacking of aromatic rings by π-π interactions.[22,23] These studies demonstrate the power of aromatic rings in triggering self-assembly and providing order and directionality of the assembly. Conveniently, the aromatic ring of phenylalanine also imparts high diamagnetic anisotropy, or susceptibility to directional alignment in a magnetic field.[15] This prior work suggests that the secondary structure of the peptide has a significant effect on its diamagnetic anisotropy. While a protein with randomly oriented phenylalanine amino acids would not exhibit directional alignment, self-assembly of these residues into secondary and tertiary structures can translate into substantial diamagnetic anisotropies at the peptide or fibril level. We calculated the molar and volumetric diamagnetic anisotropy values for a series of peptides with different residue compositions **Table S1.** Generally, the volumetric diamagnetic anisotropy increases as the number of phenylalanine in the sequence increases.
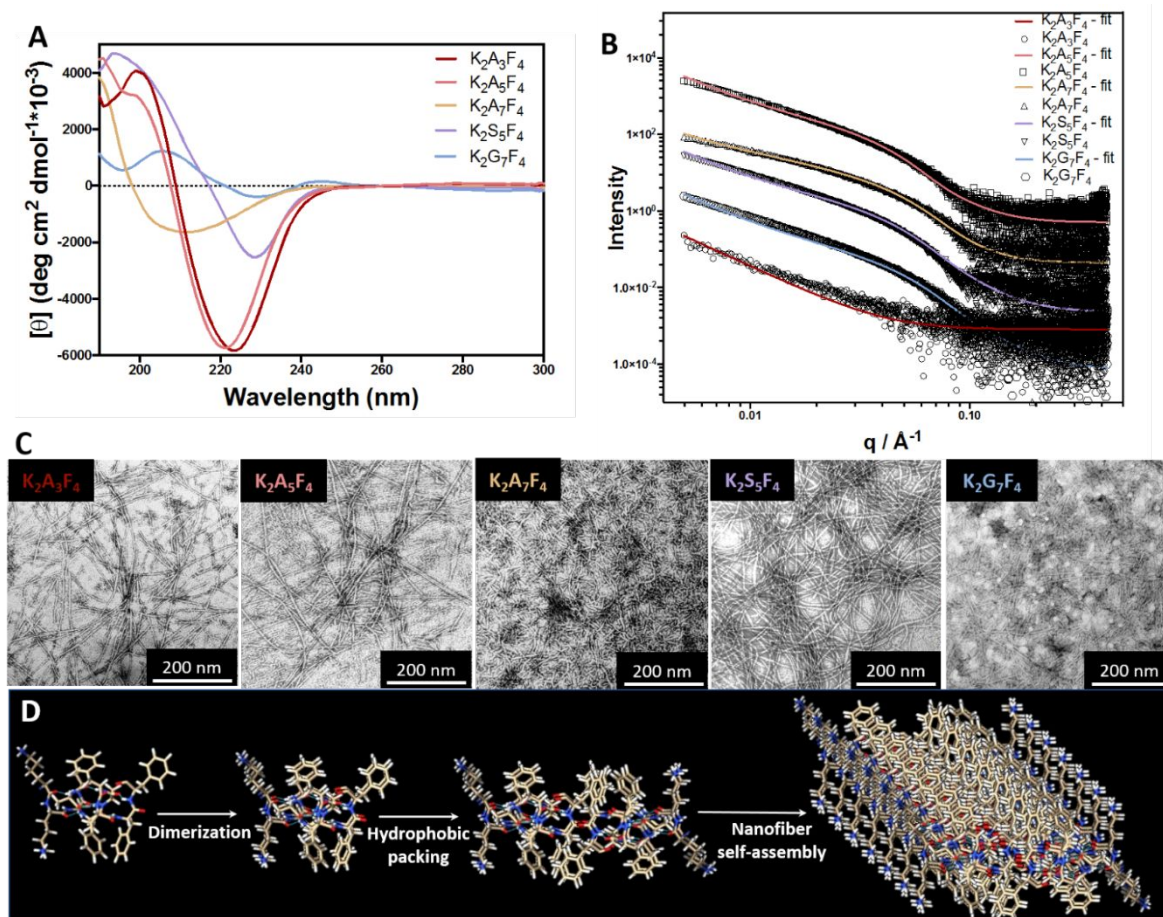
Self-assembly behavior of aromatic cationic peptides. The secondary structure of designed peptides was investigated in acidic, neutral and basic environments by circular dichroism (CD) spectroscopy. All of the peptides exhibited extended 3_1-helix or polyproline type II helix (with negative peak at 194 nm and a positive peak at 220 nm)[24] at acidic and neutral pHs, at which the lysine residues are charged (**Figure S2**). However, at pH 10, the side chain of lysine becomes less charged (**Figure S2**) and peptides with alanine linker adopt α-helical conformation, with a maximum at 180 nm and two negative minima at 200 and 212 nm. Alanine-rich peptides have been shown propensity to adopt helical conformation.[25,26] Increasing the number of alanine residues, which extends the linker length, resulted in a decrease in the intensity of the maximum peak at 180 nm, where this is more significant for $K_2A_7F_4$ peptide. The peptide containing serine residues in the linker region ($K_2S_5F_4$) showed a spectra similar to α-helix conformation with a slight shift in the second minima peak (210 -» 227 nm), which may be due to the contribution of aromatic side chains of phenylalanines[27] and hydrogen bonding between hydroxyl side chains of serine. For the peptide with glycine-containing linker ($K_2G_7F_4$), a β-sheet structure was observed at pH 10. Being achiral, glycine does not contribute significantly to the peptide's CD signal compared to the chiral amino acids at the peptide termini (K_2 and F_4).

The secondary structure of $K_2A_5F_4$ and $K_2A_3F_4$ peptides changed from being α-helix at pH 10 to β-sheet structures at pH 11 (Figure 1-A). At this pH, the peptides are mostly neutral (**Figure S2**) allowing the stacking of the phenylalanine aromatic rings as well as hydrogen bonding between the peptide backbones. FT-IR analysis of peptide solutions at pH 11 revealed mostly parallel β-sheet structures with a more intense peak at 1630 cm^{-1} compared to anti-parallel β-sheet structures at 1690 cm^{-1} (**Figure S3**, **Table S3**). Combined parallel and anti-parallel β-sheet structures were also observed by FT-IR for peptides with similar design (H-F_2ALGLAGK$_2$-OH).[28] The contribution of phenylalanine side chains in shifting the CD spectra is also visible for the $K_2A_7F_4$ and $K_2S_5F_4$ peptides. These

4

results are in agreement with the self-assembly of noncharged
diphenylalanine peptides into β-sheet structures.[29]

Table 1. Chemical structure of designed aromatic cationic peptides and their properties.

Peptide sequence	Critical Aggregation Concentration, CAC (µM)	Volumetric Diamagnetic Anisotropy (DA)*10^{-6}	Zeta potential (mV)	
			pH 7	pH 11
Ac-K$_2$A$_3$F$_4$-CONH$_2$	6.16	–	32.26 ± 0.87	2.15 ± 0.27
Ac-K$_2$A$_5$F$_4$-CONH$_2$	4.26	0.956	35.5 ± 3.87	4.90 ± 2.82
Ac-K$_2$A$_7$F$_4$-CONH$_2$	2.50	1.98	34.13 ± 0.40	2.64 ± 0.29
Ac-K$_2$S$_5$F$_4$-CONH$_2$	7.40	3.23	50.53 ± 2.45	-7.06 ± 0.51
Ac-K$_2$G$_7$F$_4$-CONH$_2$	4.40	4.51	45.06 ± 1.53	11.8 ± 0.1

Figure 1. Self-assembly behavior of cationic aromatic peptides at pH 11. (A) CD spectra; (B) SAXS patterns measured for 0.5 wt% solutions (open symbols) along with model form factor fits (solid lines). For ease of visualization, the data for $K_2S_5F_4$ has been multiplied ×10, that for $K_2A_7F_4$ ×100 and that for $K_2A_5F_4$ by ×1000. Also for clarity, only every 5th data point is plotted; (C) TEM images of 0.05 wt% of peptide solutions. (D) Proposed model for self-assembly for $K_2A_5F_4$ peptide.

The morphology of the assemblies formed by the cationic aromatic peptides are shown through TEM images taken from solutions at pH 11 (**Figure 1-C**). No defined structures were detected for $K_2A_5F_4$ at pH 7, but intertwined long fibers were observed at basic pH (pH=11). Therefore, TEM imaging was done on the remaining peptide solutions at pH 11. TEM images show nanofibrillar structures for all of the peptides but their length and density varies depending on the peptide sequence. Differences seen in the CD spectra and TEM images highlight the influence of the linker segment on the conformation and morphology of formed structures. As the alanine linker gets longer, dense nanofibers are formed but the length of the fibers gets shorter (denser fibers for $K_2A_7F_4$). In contrast, the serine linker ($K_2S_5F_4$) promotes the formation of long and well-defined nanofibers. Peptides with glycine linker ($K_2G_7F_4$) also formed long fibers, in addition to grape-like structures. SAXS analysis on the peptide solutions was also performed to further elucidate the morphology of the assemblies at pH 11. The results are presented in **Figure 1-B** along with fitted form factors based on the form factor of cylindrical nanofibrils (**Table S2**). All of the samples, except $K_2A_3F_4$, form well-defined nanofibrils with radii in the range 2.0 – 3.1 nm. This is an agreement with the TEM images, apart from $K_2A_3F_4$ which may form fibrils upon drying as part of the TEM sample preparation.

To further investigate the π-interactions of fluorenyl moieties of the peptides, fluorescence spectroscopy was used. Aromatic amino acids are intrinsically fluorescent and are mostly responsible for inherent fluorescence of proteins, with changes in their environment resulting in a fluorescence shift. Peptides solutions where excited at 210 nm[16] and a redshift (from 290 to 310 nm) in the peak of maximum fluorescence was observed at pH 11 (**Figure S4**), confirming the formation of π-π-interactions upon screening of amine groups of lysine side chains. However, this was not observed for $K_2S_5F_4$ peptide. At pH 11, only a decrease in the shoulder peak at 290 nm was detected, inferring the repulsion of deprotonated hydroxyl moieties in cancelling the π-interactions of aromatic groups.

The peptides designed in this work have an amphiphilic structure with a hydrophilic charged portion at the N-terminus and a hydrophobic aromatic segment at the C-terminus. Based on this amphiphilic structure and on the obtained experimental data, their self-assembly was proposed taken $K_2A_5F_4$ peptide as model (**Figure 1-D**). SAXS on solutions of $K_2A_5F_4$ peptide at pH 11 estimated a cylinder radius of 3.1 nm (6.2 nm in diameter). Considering a distance of 3.4 Å per residue and a linear peptide of 11 residues, the expected molecular length of a single peptide molecule is 37.4 Å. Upon charge screening (basic pH or addition of oppositely charged molecules or ions), peptides can dimerize via hydrophobic association and π-π interactions. Antiparallel association of dimers via hydrophobic effects (Figure 1-D, hydrophobic packing) results in the growth into extended nanofibers, stabilized by hydrogen bonding between peptide

backbones, with estimated diameter of ≈ 7.5 nm. This value is in accordance with the diameter obtained by SAXS.

The critical concentration for self-assembly for each peptide was also determined using the solvatochromic fluorescent dye, Nile Red[17]. Nile Red is poorly soluble in water, hence has a great tendency towards hydrophobic binding sites of molecules present in solution.[30] Therefore, the critical aggregation concentration (CAC) of peptides can be determined with Nile Red through plotting the shift in maximum wavelength or with changing in fluorescent intensity as function of the logarithm of concentration (**Figure S5**). CAC results (**Table 1**) showed that all sequences aggregate at low concentration, in the micro-molar (μM) range, and the linker segment has a slight effect on the CAC being more evident in the peptides with an alanine-based linker. As the alanine length is longer, the aromatic stacking took place at lower concentration (2.5 μM for $K_2A_7F_4$) and this increases for $K_2A_3F_4$ being 6.16 μM. Overall, the CAC of the peptides are shown to be between 2–7 μM which is lower than the CAC determined for similar peptides[28] containing only two phenylalanine residues. A higher number of phenylalanine residues enhances the hydrophobic effects and favors the self-assembly of these cationic aromatic peptides at lower concentrations.

Self-assembly of cationic aromatic peptides with hyaluronic acid (HA). Lysine residues were incorporated in the peptide design to establish electrostatic interactions with (poly)electrolytes of opposite charge. Here, peptides were self-assembled with HA in aqueous solutions, first casting HA solution on the bottom of a well plate and the peptide solution was then added on top of the HA. Different concentrations of peptides and HA were tested, but only robust membranes were formed when using 2 wt% of peptide with 1 wt% of 1.5 MDa HA

and 2 wt% of HA of lower molecular weights. Self-assembly occurred immediately and the formation of an opaque layer at the interface was observed as reported in previous studies using HA and other self-assembling peptides.[12–14,31] However, the membranes were left to grow overnight at 37 °C.

All sequences, except $K_2A_3F_4$, formed membranes at the interface of the two liquids, whereas the peptide with shorter alanine linker formed a hydrogel, acting as kind of hydrogelator. Self-assembly with higher molecular weight HA (1.5 MDa) resulted in a transparent hydrogel (**Figure 2-top**). All aromatic cationic peptides were tested with 1.5 MDa HA, as well as $K_2A_5F_4$ sequence self-assembled with different concentrations of 700 kDa and 1.5 MDa HA. As a result, membranes were formed with different thicknesses (**Figure S6**), which ranges from 18 μm for $K_2A_5F_4$ (2 wt%)/1.5 MDa HA (0.5 wt%) up to 71 μm for $K_2S_5F_4$ (2 wt%)/1.5 MDa HA (1 wt%). The higher thickness of the $K_2S_5F_4$/HA membrane is believed to be due to the presence of polar hydroxyl groups on the side chains of serine, which retain more water content compared to other membranes.

Figure 2-bottom shows a highly compact fibrillar structure for $K_2A_3F_4$/HA hydrogel. Membrane microstructure varies in density of fibers depending on the peptide sequence and the length of HA chain. The self-assembly of $K_2A_7F_4$ with HA resulted in membranes with rough surface for 1.5 MDa. The self-assembly of HA with a peptide amphiphile (PA)[14,31] and multi-domain peptides (MDPs)[12,13] into membranes showed two distinct faces, one rich in HA and the other in the peptide component. However, these membranes showed no distinct structure for both surfaces (peptide and HA sides) with randomly distributed nanofibers on both surfaces.
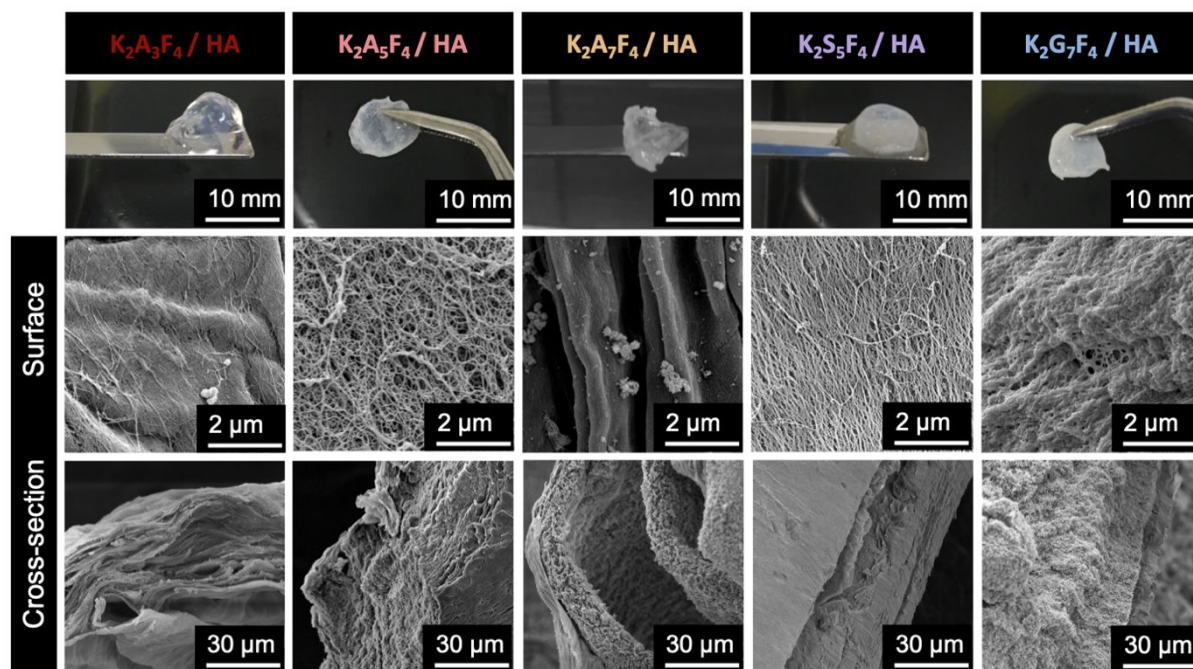
Figure 2. Photographs of hydrogels and membranes formed by self-assembly between designed cationic aromatic peptides and HA and their nanofibrous structure revealed by SEM images.

Analysis of the cross-section also shows nanofibrous structure and no evident layer showing the interface between the two mixed

components (**Figure 2-bottom**). SAXS was also used to investigate the nanostructure organization of the membranes.

SAXS data for dried membranes is shown in **Figure 3-A**. $K_2A_5F_4$ and $K_2S_5F_4$ membranes show well-developed Bragg peaks at $q = 0.087$ Å^{-1} and $q = 0.099$Å^{-1} respectively, corresponding to average mesh sizes within the membranes of $d = 73$ Å and $d = 63$ Å respectively. SAXS from $K_2A_7F_4$ and $K_2G_7F_4$ also shows Bragg peaks, but they are broader than for the other two samples corresponding to spacings of $d = 56$ Å (the peak for $K_2A_7F_4$ is asymmetric, indicating a population of structures with longer spacings in addition). SAXS on hydrated as well as rehydrated membranes was also performed (**Figure S7)**. The data for $K_2A_7F_4$ and $K_2G_7F_4$ shows very distinct structure in hydrated and dried states, with reversibility on hydration (the SAXS profiles show the same shape as the initial profile for the hydrated sample, with only a loss of intensity). The initial SAXS profiles for hydrated samples show fibril form factor features, however for the dried membranes, clearly defined Bragg peaks are observed at $q^* = 0.115$ Å^{-1} and $q = 0.23$ A^{-1} (close to $2q^*$) for $K_2A_7F_4$ (**Figure S7**) which indicates a lamellar structure with spacing of $d = 54.6$ Å. Upon rehydration, the SAXS profile reverts to the same initial form factor shape. Similarly, the first SAXS profile for dried $K_2G_7F_4$ (**Figure S7**) shows Bragg peaks at $q = 0.103$ Å^{-1} and $q = 0.21$ Å^{-1}, corresponding to a lamellar structure with $d = 61.0$ Å. Considering a peptide layer of around 40 Å thick, if highly interdigitated, and the total lamellar spacing, a 20 Å thick HA layer is estimated, and corresponding to four to six HA chains. Some order in this pattern is lost subsequently, but the intensity profile in the hydrated state is very similar after multiple re-hydrations as shown in **Figure S7**. In contrast to $K_2A_7F_4$, the SAXS profile in the hydrated state retains a Bragg peak, i.e. a structure factor peak with $q^* = 0.077$ Å^{-1} corresponding to a domain spacing of $d = 82$ Å. There is a weak second order peak near $\sqrt{3}\ q^*$, which suggests remarkable hexagonal order of fibrils in the hydrated state for the $K_2G_7F_4$/HA membrane. SAXS on membranes obtained by self-assembly of HA and a positively charged peptide amphiphile revealed Bragg peaks in the scattering profile indicative of a cubic phase.[32]

Mechanical testing of cationic aromatic peptide/HA biomaterials. The mechanical characterization of $K_2X_nF_4$/HA membranes was performed by tensile testing (**Figure 3-C-E**). In a tensile test, the uniaxial forces are used to stretch the clamped sample with known dimensions and measures the elongation versus applied load. The stress-strain curves show an evident dependence on the linker region used in the peptide design, illustrating either highly elastic soft membranes ($K_2S_5F_4$/HA stretched up to 3 times its initial length) or stronger but brittle membranes ($K_2A_5F_4$/HA).

Among the membranes made from peptides with different linkers, $K_2A_5F_4$/HA presents the highest elastic modulus (0.02 MPa) (**Figure 3-D**), which is lower compared to the PA/HA membranes with tensile strength of 0.9 MPa in hydrated state[31]. This can be due to the lack of hierarchical organization observed for the cationic aromatic peptide/HA membranes. However, these membranes can sustain stresses of around 1.2 MPa until failure or stretch up to twice their length. Therefore, it is possible to obtain membranes with tunable mechanical properties through the design of the peptide component as well as through the changes in the concentration of the components.

The membranes were imaged after tensile testing to check their microstructure at the breaking point. The microstructure was affected by the stretching of the membranes, showing fibers are more aligned in the pulling direction at the breaking region compared to the mid-region of the membrane (**Figure S8**). The fiber alignment post stretching is seen for all membranes, but for the $K_2S_5F_4$/HA membrane the stretching-induced alignment resulted in the formation of fiber bundles as this is the most stretchable among the tested membranes.
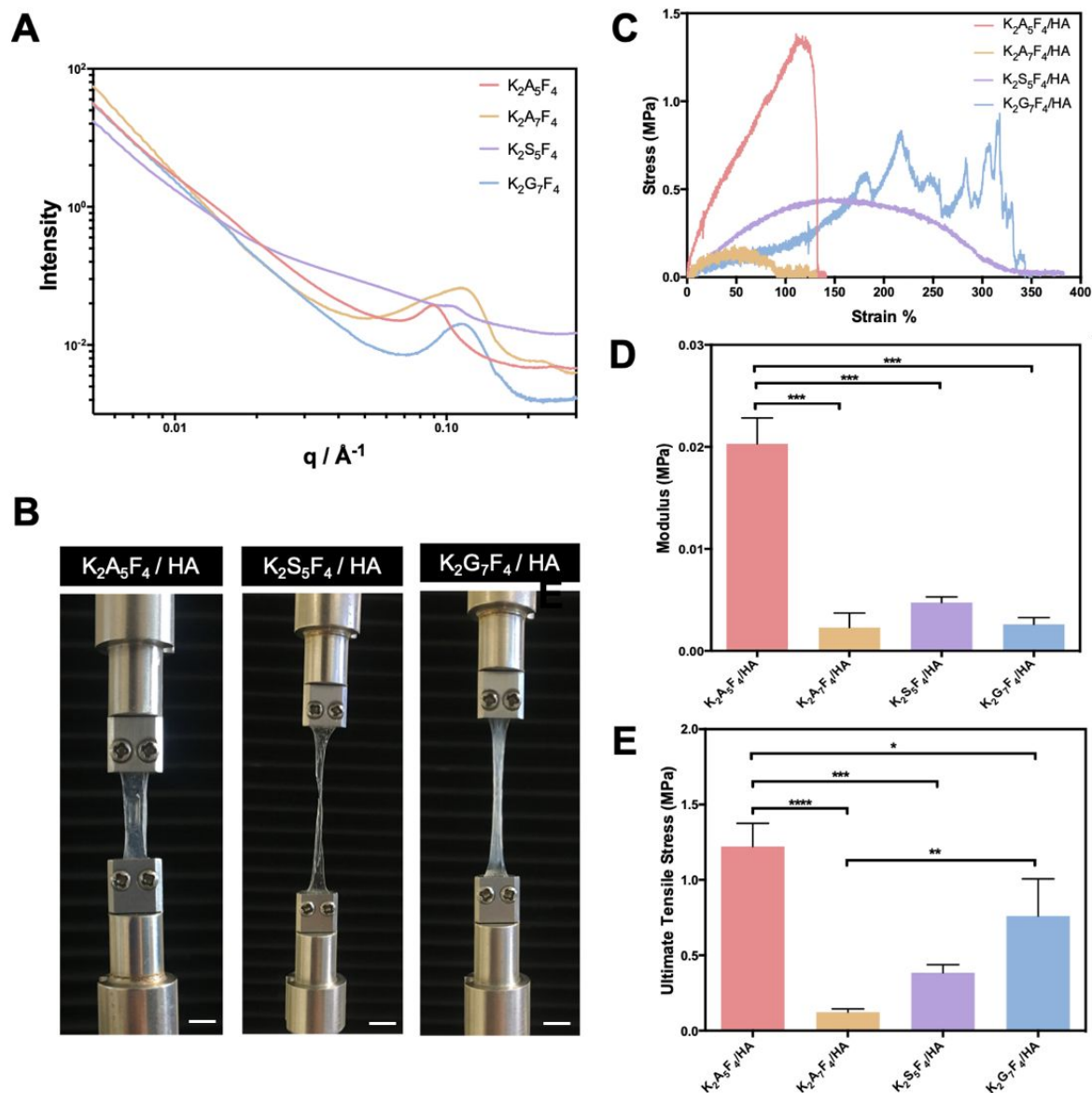
Figure 3. Structural and mechanical analysis of the peptide/HA membranes: (A) SAXS measurements on dried membranes; (B) Images showing membranes clamped between two grips allowing uniaxial stretching (scale bar: 4.5 mm); (C) Stress-strain curves of tensile tested membranes, (D) Tensile modulus and (E) Ultimate tensile stress.

The mechanical properties of the $K_2A_3F_4$/HA hydrogels were obtained in a oscillatory rheometer using HA of two molecular weights (700 kDa and 1.5 MDa) to assess the effect of HA length on the stiffness of the hydrogels. The linear viscoelastic region (LVER) was obtained from amplitude sweeps for each group of hydrogels. Both $K_2A_3F_4$/700 kDa HA and $K_2A_3F_4$/1.5 MDa HA maintained their linearity up to 5% strain at frequency of 1 Hz. In order to assess the stiffness of the hydrogels, frequency sweeps were measured at 0.1% strain (in the LVER) with changing in frequency. In both graphs (**Figure S9**), the storage modulus exceeds the loss modulus showing typical behavior of a gel system. The effect of HA Mw on the stiffness of the hydrogels showed higher elastic modulus for $K_2A_3F_4$/1.5 MDa HA gel (1.8 kPa) compared to $K_2A_3F_4$/700 kDa HA (0.6 kPa), indicating the versatility of the system to obtain hydrogels with different stiffness.

Magnetic alignment of peptide nanofibers during membrane assembly. External fields (electric, magnetic) have been used to direct peptide self-assembly.[19] For example, the effect of electric field on the self-assembly of oppositely charged molecules (anionic HA and cationic peptide amphiphile) was investigated.[33] Electrical field was applied to promote or prevent HA diffusion and shown to affect the kinetics of membrane formation and their final properties (nanostructure organization, thickness, and mechanical properties).

Considering the diamagnetic anisotropy of the aromatic rings of the phenylalanine residues, and based on the previous work showing the alignment of diphenylalanine nanotubes under magnetic field,[6] we exploited the application of magnetic field during formation of the membrane. As the peptide is expected to play a major role in the magnetic alignment of the fibers, the secondary structure of peptides were first analyzed at pH 7 and 11 after being exposed to a 1 T magnetic field for 24 hours

(**Figure S10**). The magnetic field had the most effect on peptide conformation at pH 11, where the π-π stacking is stronger. The β-sheet structure of the peptides at pH 11 is affected after exposure to a 1 T field suggesting the orientation of aromatic rings with the field disturbed the β-sheet configuration. At pH 7, a slight shift and decrease in the minimum peak at 190 nm is evident. Overall, CD results showed that the magnetic field affected the secondary structures of the peptides.
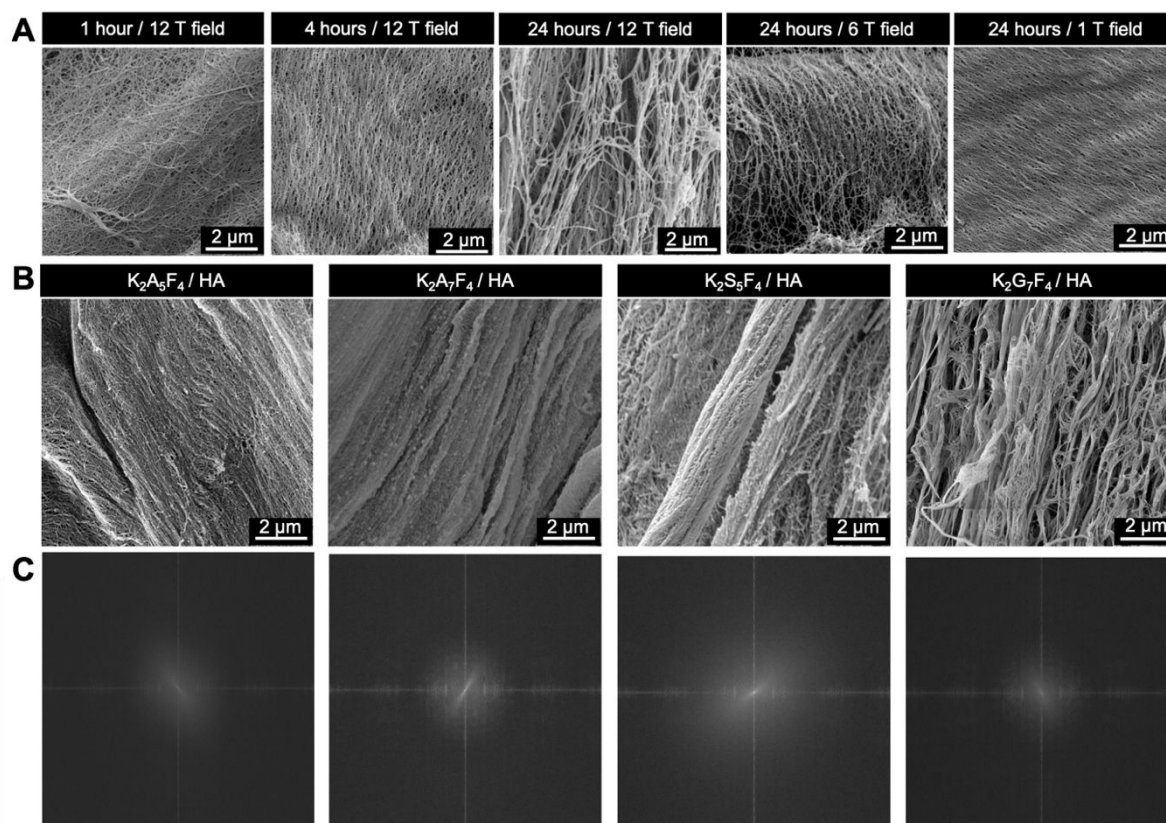
Figure 4. Effect of magnetic field during the membrane assembly on nanofiber alignment: (A) SEM images showing the surface of $K_2A_5F_4$/HA membranes formed under a magnetic field for different periods of time and of intensity and (B) membranes assembled with the designed peptides in the presence of 1 T magnetic field for 24 h ; (C) FFT analysis of aligned fibers membranes.

The effect of magnetic field intensity and exposure time was investigated on the $K_2A_5F_4$/1.5 MDa HA system at 1 and 6 T for 24 hours and 12 T for 1, 4 and 24 hours (**Figure 4-A**). Exposure time affected the alignment and only 1 hour exposing time is not enough to obtain uniform fiber alignment on the membrane. Fibers can be aligned at lower magnetic field, such as 1 T, if exposure time is longer (24 hours). The nanofiber alignment was confirmed by microstructure analysis (SEM) for all membranes at 1 T magnetic field (**Figure 4-B, C**). A peptide amphiphile (PA, $C_{16}V_3A_3K_3$) previously used to form membranes with HA, but not containing aromatic residues, was used as a control peptide. The PA/HA membranes were also formed under a 12 T magnetic field for 24 hours. Randomly distributed fibers of PA/HA were observed confirming the role of aromatic groups in the nanofiber alignment (**Figure S11-A**). The aligned fibers were maintained after incubating in water for one month, indicating their stability (**Figure S11-B**). The nanofiber organization of the membranes was also analyzed by polarized light microscopy. Due to their fibrillar characteristics, they showed structural birefringent properties.[34,35] **Figure S11-C** shows the alignment of fibers enhanced the birefringence of the $K_2A_5F_4$/HA membrane in one direction compared to the membrane without magnetic field exposure. To further analyze the direction of the fibers, a graphite rod was used as a probe to confirm that fibers are aligned in the direction of the magnetic field. **Figure S12** shows the SEM images with the aligned fibers in the direction of the graphite pencil lead. Having the graphite on the peptide surface, the HA and peptide sides were identified.

Attachment of MSCs cultured on aligned peptide/HA membranes. In order to maintain proper function and morphology, cells need to attach to their surrounding environment. This attachment can be either binding to the ECM or to other cells.[36] Specific peptide segments in ECM proteins (e.g. RGDS in fibronectin) are known to act as anchoring points for binding to cell surface receptors (integrins) leading to the formation of focal adhesions.[37,38] Here, we have investigated the effect of nanofiber alignment on the attachment of mesenchymal stem cells (MSCs) onto the various membranes.

The effect of nanofiber alignment on cell attachment was first studied on membranes formed under 1 T magnetic field and using serum-containing medium. Fluorescent microscopy images show the spreading and morphology of MSCs (**Figure 5-A**) on aligned and non-aligned membranes. Compared to cells on non-aligned membranes, MSCs elongated on the membranes in the direction of the aligned nanofibers, and this elongation is more evident for $K_2G_7F_4$/HA membranes ($K_2G_7F_4$ with highest diamagnetic anisotropy, **Table S1**). Cell attachment was also assessed in

10

serum-free conditions using $K_2A_5F_4$/HA membranes and also on membranes formed with 90% of $K_2A_5F_4$ and 10% of RGDS-$K_2A_5F_4$ peptide. **Figure 5-B** compares the density and aspect ratio of cells cultured on $K_2A_5F_4$/HA membranes in presence or absence of serum, and on RGDS-containing membranes in serum-free medium. It is clear that the presence of FBS has a significant role on cell adhesion and the fiber alignment tends to favor cell attachment compared to non-aligned membranes, in particular when membranes contain the RGDS cell-adhesive sequence. We postulate that the magnetic alignment of the nanofibers promoted the presentation of the RGDS epitopes on the surface, hence cell anchorage increased compared to non-aligned membranes.

Further investigation on the interaction of MSCs with these membranes by SEM analysis revealed the spreading of cells along the nanofibrous network of the membranes. Cells showed lamellipodia and filopodia, which are more extended in the direction of aligned fibers (**Figure 5-C**). Furthermore, cells are able to pull the nanofibers and seem to remodel these soft supramolecular membranes. Through the incorporation of RGDS sequence, membranes were able to promote the adhesion of MSCs under serum-free conditions and nanofiber alignment directed their spreading.

11
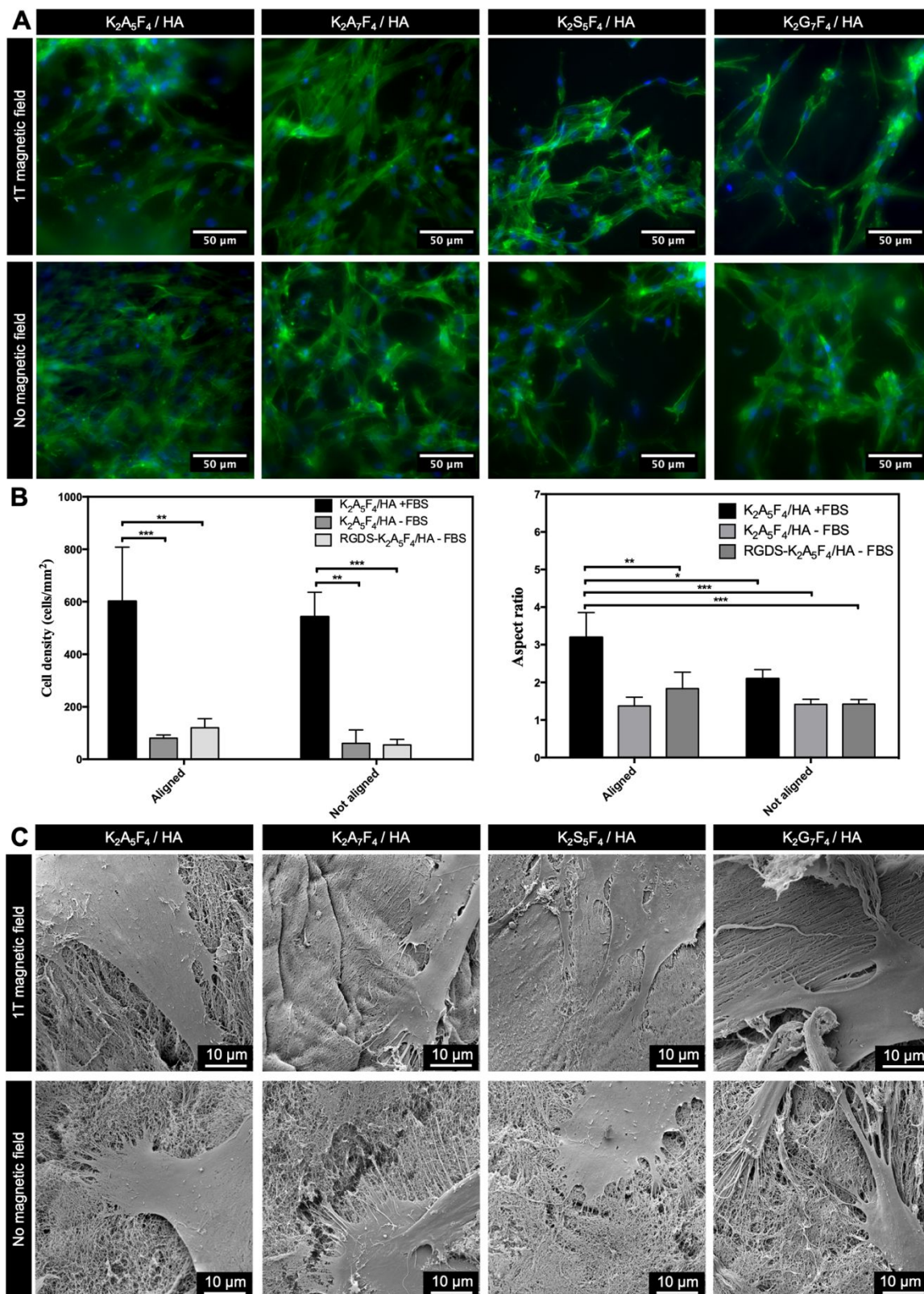
Figure 5. Cell behavior on the various peptide/HA membranes: (A) Fluorescence microscopy images of hMSCs cultured on aligned and non-aligned membranes (serum-containing cell media) for 24 hours; (B) Graphs displaying cell density (left) and cell aspect ratio (right) comparing culturing conditions (in presence of serum and serum-free) as well as the effect of RGDS on cell attachment on $K_2A_5F_4$/HA membranes; (C) SEM micrographs showing the cell interaction with the membrane nanofibrous surface (24 hrs) in the presence of serum.

CONCLUSION

Novel aromatic cationic peptides have been designed for supramolecular assembly with hyaluronic acid into hydrogels or membranes. The designed peptides can adopt different secondary structures depending on the pH and their self-assembly is driven by electrostatic screening followed by π-π stacking of phenylalanine residues. The linker segment in the peptide sequence was shown to affect the mechanical properties of the obtained membranes. The modulus of the resulting materials (hydrogels or membranes) can be tuned through the HA molecular size and concentration of components. Owing to the diamagnetic anisotropy of phenylalanine, the peptide nanofibers in the membranes were able to align while forming in the presence of magnetic field. The alignment of fibers enhanced the attachment of mesenchymal stem cells. These findings suggest the potential of these self-assembled membranes as cell culture substrates to study the effect of biochemical and physical (nanofiber organization) signaling on stem cell behavior.

ASSOCIATED CONTENT

Supporting Information

The Supporting Information is available free of charge on the ACS Publications website.

Peptide characterization (HPLC, ESI-MS, CD, fluorescence and FTIR spectra; zeta potential, DA calculation, SAXS, CAC determination); Membrane characterization (thickness, SAXS data, SEM and polarized microscopy images) (PDF)

AUTHOR INFORMATION

Corresponding Author

* Helena S. Azevedo - School of Engineering & Materials Science, Queen Mary University of London, Mile End Road, London E1 4NS, UK; orcid.org/0000-0002-5470-1844; Tel: +44(0)20 7882 5502; E-mail: h.azevedo@qmul.ac.uk

Present Addresses

†If an author's address is different than the one given in the affiliation line, this information may be included here.

Author Contributions

The manuscript was written through contributions of all authors. All authors have given approval to the final version of the manuscript.

Funding Sources

Notes

The authors declare no competing financial interest.

ACKNOWLEDGMENTS

ABBREVIATIONS

CAC, critical aggregation concentration; CD, circular dichroism; DA, diamagnetic anisotropy; FTIR, Fourier Transform Infrared; HA, hyaluronic acid; HPLC, high performance liquid chromatography; hMSCs, human-derived mesenchymal stem cells; SAXS, small angle X-ray scattering; SEM, scanning electron microscopy; TEM, transmission electron microscopy.

1
2
3
4
5
6
7
8
9
10
11
12
13
14
15
16
17
18
19
20
21
22
23
24
25
26
27
28
29
30
31
32
33
34
35
36
37
38
39
40
41
42
43
44
45
46
47
48
49
50
51
52
53
54
55
56
57
58
59
60

REFERENCES

(1) van der Gucht, J. Grand Challenges in Soft Matter Physics. *Front. Phys.* **2018**, *6*, 87.

(2) Yuan, C.; Ji, W.; Xing, R.; Li, J.; Gazit, E.; Yan, X. Hierarchically Oriented Organization in Supramolecular Peptide Crystals. *Nat. Rev. Chem.* **2019**, 1–22.

(3) Lum, G. Z.; Ye, Z.; Dong, X.; Marvi, H.; Erin, O.; Hu, W.; Sitti, M. Shape-Programmable Magnetic Soft Matter. *Proc. Natl. Acad. Sci.* **2016**, *113* (41), E6007–E6015.

(4) Erb, R. M.; Martin, J. J.; Soheilian, R.; Pan, C.; Barber, J. R. Actuating Soft Matter with Magnetic Torque. *Adv. Funct. Mater.* **2016**, *26* (22), 3859–3880.

(5) Smal, N.; Löwik, D. W. P. M. Magnetic Fields to Align Natural and Synthetic Fibers. In *Self-assembling Biomaterials*; Elsevier, 2018; pp 321–340.

(6) A. Hill, R. J.; Sedman, V. L.; Allen, S.; Williams, P.; Paoli, M.; Adler-Abramovich, L.; Gazit, E.; Eaves, L.; Tendler, S. J. B. Alignment of Aromatic Peptide Tubes in Strong Magnetic Fields. *Adv. Mater.* **2007**, *19* (24), 4474–4479.

(7) Löwik, D. W. P. M.; Shklyarevskiy, I. O.; Ruizendaal, L.; Christianen, P. C. M.; Maan, J. C.; van Hest, J. C. M. A Highly Ordered Material from Magnetically Aligned Peptide Amphiphile Nanofiber Assemblies. *Adv. Mater.* **2007**, *19* (9), 1191–1195.

(8) Kwon, S.; Kim, B. J.; Lim, H.-K.; Kang, K.; Yoo, S. H.; Gong, J.; Yoon, E.; Lee, J.; Choi, I. S.; Kim, H. Magnetotactic Molecular Architectures from Self-Assembly of β-Peptide Foldamers. *Nat. Commun.* **2015**, *6*, 8747.

(9) Wallace, M.; Cardoso, A. Z.; Frith, W. J.; Iggo, J. A.; Adams, D. J. Magnetically Aligned Supramolecular Hydrogels. *Chem. Eur. J.* **2014**, *20* (50), 16484–16487.

(10) Torbet, J.; Malbouyres, M.; Builles, N.; Justin, V.; Roulet, M.; Damour, O.; Oldberg, Å.; Ruggiero, F.; Hulmes, D. J. S. Orthogonal Scaffold of Magnetically Aligned Collagen Lamellae for Corneal Stroma Reconstruction. *Biomaterials* **2007**, *28* (29), 4268–4276.

(11) Klara, S. S.; Saboe, P. O.; Sines, I. T.; Babaei, M.; Chiu, P.-L.; DeZorzi, R.; Dayal, K.; Walz, T.; Kumar, M.; Mauter, M. S. Magnetically Directed Two-Dimensional Crystallization of OmpF Membrane Proteins in Block Copolymers. *J. Am. Chem. Soc.* **2016**, *138* (1), 28–31.

(12) Mendes, A. C.; Smith, K. H.; Tejeda-Montes, E.; Engel, E.; Reis, R. L.; Azevedo, H. S.; Mata, A. Co-Assembled and Microfabricated Bioactive Membranes. *Adv. Funct. Mater.* **2013**, *23* (4), 430–438.

(13) Ribeiro, S.; Radvar, E.; Shi, Y.; Borges, J.; Pirraco, R. P.; Leonor, I. B.; Mano, J. F.; Reis, R. L.; Mata, Á.; Azevedo, H. S. Nanostructured Interfacial Self-Assembled Peptide-Polymer Membranes for Enhanced Mineralization and Cell Adhesion. *Nanoscale* **2017**, *9* (36), 13670–13682.

(14) Ferreira, D. S.; Marques, A. P.; Reis, R. L.; Azevedo, H. S. Hyaluronan and Self-Assembling Peptides as Building Blocks to Reconstruct the Extracellular Environment in Skin Tissue. *Biomater. Sci.* **2013**, *1* (9), 952–964.

(15) Babaei, M.; Jones, I. C.; Dayal, K.; Mauter, M. S. Computing the Diamagnetic Susceptibility and Diamagnetic Anisotropy of Membrane Proteins from Structural Subunits. *J. Chem. Theory Comput.* **2017**, *13* (6), 2945–2953.

(16) Yu, Z.; Tantakitti, F.; Palmer, L. C.; Stupp, S. I. Asymmetric Peptide Nanoribbons. *Nano Lett.* **2016**, *16* (11), 6967–6974.

(17) Shi, Y.; Hu, Y.; Ochbaum, G.; Lin, R.; Bitton, R.; Cui, H.; Azevedo, H. S. Enzymatic Activation of Cell-Penetrating Peptides in Self-Assembled Nanostructures Triggers Fibre-to-Micelle Morphological Transition. *Chem. Commun.* **2017**, *53* (52), 7037–7040.

(18) Hutchinson, J. A.; Hamley, I. W.; Edwards-Gayle, C. J. C.; Castelletto, V.; Piras, C.; Cramer, R.; Kowalczyk, R.; Seitsonen, J.; Ruokolainen, J.; Rambo, R. P. Melanin Production by Tyrosinase Activity on a Tyrosine-Rich Peptide Fragment and PH-Dependent Self-Assembly of Its Lipidated Analogue. *Org. Biomol. Chem.* **2019**, *17* (18), 4543–4553.

(19) Mendes, A. C.; Baran, E. T.; Reis, R. L.; Azevedo, H. S. Self-assembly in Nature: Using the Principles of Nature to Create Complex Nanobiomaterials. *Wiley Interdiscip. Rev. Nanomedicine Nanobiotechnology* **2013**, *5* (6), 582–612.

(20) Aulisa, L.; Dong, H.; Hartgerink, J. D. Self-Assembly of Multidomain Peptides: Sequence Variation Allows Control over Cross-Linking and Viscoelasticity. *Biomacromolecules* **2009**, *10* (9), 2694–2698.

(21) Paramonov, S. E.; Jun, H.-W.; Hartgerink, J. D. Self-Assembly of Peptide− Amphiphile Nanofibers: The Roles of Hydrogen Bonding and Amphiphilic Packing. *J. Am. Chem. Soc.* **2006**, *128* (22), 7291–7298.

(22) Reches, M.; Gazit, E. Casting Metal Nanowires within Discrete Self-Assembled Peptide Nanotubes. *Science (80-.).* **2003**, *300* (5619), 625–627.

(23) Adler-Abramovich, L.; Vaks, L.; Carny, O.; Trudler, D.; Magno, A.; Caflisch, A.; Frenkel, D.; Gazit, E. Phenylalanine Assembly into Toxic Fibrils Suggests Amyloid Etiology in Phenylketonuria. *Nat. Chem. Biol.* **2012**, *8* (8), 701–706.

(24) Kelly, S. M.; Jess, T. J.; Price, N. C. How to Study Proteins by Circular Dichroism. *Biochim. Biophys. Acta (BBA)-Proteins Proteomics* **2005**, *1751* (2), 119–139.

(25) Smith, S. J.; Du, K.; Radford, R. J.; Tezcan, F. A. Functional, Metal-Based Crosslinkers for α-Helix Induction in Short Peptides. *Chem. Sci.* **2013**, *4* (9), 3740–3747.

(26) Shi, Y.; Ferreira, D. S.; Banerjee, J.; Pickford, A. R.; Azevedo, H. S. Tuning the Matrix Metalloproteinase-1 Degradability of Peptide Amphiphile Nanofibers through Supramolecular Engineering. *Biomater. Sci.* **2019**, *7* (12), 5132–5142.

(27) Krittanai, C.; Johnson Jr, W. C. Correcting the Circular Dichroism Spectra of Peptides for Contributions of Absorbing Side Chains. *Anal. Biochem.* **1997**, *253* (1), 57–64.

(28) Son, J.; Kalafatovic, D.; Kumar, M.; Yoo, B.; Cornejo, M. A.; Contel, M.; Ulijn, R. V. Customizing Morphology, Size, and Response Kinetics of Matrix Metalloproteinase-Responsive Nanostructures by Systematic Peptide Design. *ACS Nano* **2019**, *13* (2), 1555–1562.

(29) Mahler, A.; Reches, M.; Rechter, M.; Cohen, S.; Gazit, E. Rigid, Self-assembled Hydrogel Composed of a Modified Aromatic Dipeptide. *Adv. Mater.* **2006**, *18* (11), 1365–1370.

(30) Stuart, M. C. A.; van de Pas, J. C.; Engberts, J. B. F. N. The Use of Nile Red to Monitor the Aggregation Behavior in Ternary Surfactant–Water–Organic Solvent Systems. *J. Phys. Org. Chem.* **2005**, *18* (9), 929–934.

(31) Capito, R. M.; Azevedo, H. S.; Velichko, Y. S.; Mata, A.; Stupp, S. I. Self-Assembly of Large and Small Molecules into Hierarchically Ordered Sacs and Membranes. *Science (80-.).* **2008**, *319* (5871), 1812–1816.

(32) Bitton, R.; Chow, L. W.; Zha, R. H.; Velichko, Y. S.; Pashuck, E. T.; Stupp, S. I. Electrostatic Control of Structure in Self-Assembled Membranes. *Small* **2014**, *10*

14

(3), 500–505.

(33) Velichko, Y. S.; Mantei, J. R.; Bitton, R.; Carvajal, D.; Shull, K. R.; Stupp, S. I. Electric Field Controlled Self-Assembly of Hierarchically Ordered Membranes. *Adv. Funct. Mater.* **2012**, *22* (2), 369–377.

(34) Zhang, S.; Greenfield, M. A.; Mata, A.; Palmer, L. C.; Bitton, R.; Mantei, J. R.; Aparicio, C.; De La Cruz, M. O.; Stupp, S. I. A Self-Assembly Pathway to Aligned Monodomain Gels. *Nat. Mater.* **2010**, *9* (7), 594-601.

(35) Murphy, D. B.; Spring, K. R.; Fellers, T. J.; Davidson, M. W. Principles of Birefringence https://www.microscopyu.com/techniques/polarized-light/principles-of-birefringence.

(36) Ruoslahti, E. RGD and Other Recognition Sequences for Integrins. *Annu. Rev. Cell Dev. Biol.* **1996**, *12* (1), 697–715.

(37) Storrie, H.; Guler, M. O.; Abu-Amara, S. N.; Volberg, T.; Rao, M.; Geiger, B.; Stupp, S. I. Supramolecular Crafting of Cell Adhesion. *Biomaterials* **2007**, *28* (31), 4608–4618.

(38) Hirano, Y.; Okuno, M.; Hayashi, T.; Goto, K.; Nakajima, A. Cell-Attachment Activities of Surface Immobilized Oligopeptides RGD, RGDS, RGDV, RGDT, and YIGSR toward Five Cell Lines. *J. Biomater. Sci. Polym. Ed.* **1993**, *4* (3), 235–243.

Table of contents